PNAS
www.pnas.org

SUPPPORTING INFORMATION (SI APPENDIX)

Mapping the functional anatomy of Orai1 transmembrane domains for CRAC channel gating

Priscilla S.-W. Yeung, Megumi Yamashita, Christopher E. Ing, Régis Pomès, Douglas M. Freymann, and Murali Prakriya

METHODS

Cells. HEK293 cells were maintained in suspension at 37°C with 5% CO_2 in CD293 medium supplemented with 4 mM GlutaMAX (Invitrogen). For imaging and electrophysiology, cells were plated onto poly-L-lysine coated coverslips one day before transfection and grown in a medium containing 44% DMEM (Corning), 44% Ham's F12 (Corning), 10% fetal bovine serum (HyClone), 2 mM glutamine, 50 U/ml penicillin and 50 µg/ml streptomycin.

Plasmids and transfections. The Orai1 mutants employed for electrophysiology were engineered into either the previously described C-terminal myc-tagged Orai1 construct (MO70 Orai1) in the bicistronic expression vector pMSCV-CITE-eGFP-PGK-Puro (1) or a pEYFP-N1 vector (Clonetech) to produce C-terminally tagged Orai1-YFP proteins (2). No differences in current density were observed between the two constructs. mCherry-STIM1 and CFP-CAD were kind gifts of Dr. R. Lewis (Stanford University, USA). All mutants were generated by the QuikChange Mutagenesis Kit (Agilent Technologies) and the mutations were confirmed by DNA sequencing. For electrophysiology, the indicated Orai1 constructs were transfected into HEK293 cells either alone (200 ng DNA per coverslip) or together with STIM1 (100 ng Orai1 and 500 ng STIM1 DNA per coverslip). For FRET and confocal microscopy experiments, cells were transfected with Orai1-YFP alone (200 ng DNA per coverslip) or with CFP-CAD constructs (100 ng each per coverslip). All transfections were performed using Lipofectamine 2000 (Thermo Fisher Scientific) 24-48 hours prior to electrophysiology or imaging experiments.

Solutions and Chemicals. The standard extracellular Ringer's solution used for electrophysiological experiments contained 130 mM NaCl, 4.5 mM KCl, 20 mM $CaCl_2$, 10 mM tetraethylammonium chloride (TEA-Cl), 10 mM D-glucose, and 5 mM HEPES (pH 7.4 with NaOH). For the FRET and confocal imaging studies, the Ringer's solution contained 2 mM $CaCl_2$ and 150 mM NaCl with the other components as above. The DVF Ringer's solution contained 150 mM NaCl, 10 mM HEDTA, 1 mM EDTA, 10 mM TEA-Cl and 5 mM HEPES (pH 7.4). The internal solution contained: 135 mM Cs aspartate, 8 mM $MgCl_2$, 8 mM Cs-BAPTA, and 10 mM HEPES (pH 7.2 with CsOH).

Electrophysiology. Currents were recorded in the standard whole-cell configuration at room temperature on an Axopatch 200B amplifier (Molecular Devices) interfaced to an ITC-18 input/output board (Instrutech). Routines developed by R. S. Lewis (Stanford) on the Igor Pro software (Wavemetrics) were employed for stimulation, data acquisition and analysis. Data are corrected for the liquid junction potential of the pipette solution relative to Ringer's in the bath (-10 mV). The holding potential was +30 mV. The standard voltage stimulus consisted of a 100-ms step to –100 mV followed by a 100-ms ramp from –100 to +100 mV applied at 1 s intervals. I_{CRAC} was typically activated by passive depletion of ER Ca^{2+} stores by intracellular dialysis of 8 mM BAPTA. All currents were acquired at 5 kHz and low pass filtered with a 1 kHz Bessel filter built into the amplifier. All data were corrected for leak currents collected in 100-200 μM $LaCl_3$.

Data analysis. Analysis of current amplitudes was typically performed by measuring the peak currents during the -100 mV pulse. Specific mutants were categorized as gain-of-function if their currents exceeded 2 pA/pF, which is more than ten times the current density of WT Orai1 without STIM1. Reversal potentials were measured from the average of several leak-subtracted sweeps in each cell. Fractional blockade of current was quantified as: blockade=$(1-I_b/I_{Ctrl})$, where I_b is the Orai1 current in the presence of Cd^{2+}, and I_{Ctrl} is the Orai1 current prior to application of the blocker. The fold increase in current following whole-cell break-in was calculated by measuring the peak of the STIM1-gated current amplitude at 300 s or later divided by the amount of constitutive current seen at the time of whole-cell break-in (t=0). In cells where 100-200 μM $LaCl_3$

did not completely block the current, the raw non-leak subtracted current amplitude was used as the baseline current at whole-cell break-in to compare with the current amplitude after store-depletion, with the assumption that most of the standing current arose from the over-expressed open mutant rather than from other sources.

FRET microscopy. HEK293 cells transfected with Orai1-YFP and CFP-CAD DNA constructs were imaged using wide-field epifluorescence microscopy on an IX71 inverted microscope (Olympus, Center Valley, PA). Cells were imaged with a 60X oil immersion objective (UPlanApo NA 1.40), a 175 W Xenon arc lamp (Sutter, Novatao, CA), and excitation and emission filter wheels (Sutter, Novato, CA). At each time point, three sets of images (CFP, YFP, and FRET) were captured on a cooled EM-CCD camera (Hamamatsu, Bridgewater, NJ) using optical filters specific for the three images as previously described. Image acquisition and analysis was performed with SlideBook software (Imaging Innovations Inc., Denver, CO). Images were captured at exposures of 100-500 ms with 1X1 binning. Lamp output was attenuated to 25% by a 0.6 ND filter in the light path to minimize photobleaching. All experiments were performed at room temperature.

FRET analysis was performed as previously described (2). The microscope-specific bleed-through constants (a=0.12; b=0.008; c=0.002 and d=0.33) were determined from cells expressing cytosolic CFP or YFP alone. The apparent FRET efficiency was calculated from background-subtracted images using the formalism (3):

$$E_{FRET} = \frac{F_c}{F_c + GI_{DD}}$$

where $F_c = I_{DA} - aI_{AA} - dI_{DD}$

I_{DD}, I_{AA} and I_{DA} refer to the background subtracted CFP, YFP, and FRET images, respectively. The instrument dependent G factor had the value 1.85 ± 0.1. E-FRET analysis was restricted to cells with YFP/CFP ratios in the range of 2-6 to ensure that E-FRET was compared across identical acceptor to donor ratios, and measurements were restricted to regions of interest drawn at the plasma membrane.

Confocal microscopy. HEK293 cells expressing various Orai1-YFP mutants and CFP-CAD were imaged on an Andor XDI Revolution spinning-disk confocal microscope equipped with a 100X oil immersion objective. Cells were maintained at 37°C with 5% CO_2. Fluorophores were excited with 445 nm (CFP) and 515 nm (YFP) laser diodes with the intensity of laser light attenuated to 15-40% for CFP and 5-30% for YFP. Images were obtained at 512X512 pixels at an exposure of 200-500 ms per frame and a slice thickness of 0.8 μm. An average of four frames were used for each image. Images analysis was performed using NIH ImageJ software (NIH, Bethesda, MD).

Molecular dynamics simulations. Molecular models were constructed using the crystal structure of the *Drosophila melanogaster* Orai1 channel (4HKR) (4). Missing residues of the M1-M2 loop (amino acids 181 to 190) and the M2-M3 loop (amino acids 220 to 235) were modelled *de novo* using MODELLER (5). System preparation was performed using CHARMM-GUI membrane builder (6). The C terminus was truncated at residue 329 for all chains and the N and C terminus were acetylated and amidated, respectively. The protein was embedded within a hydrated 1-palmitoyl,2-oleoyl-sn-glycero-3-phosphocholine (POPC) bilayer with 150 mM NaCl to obtain a hexagonal cell with box vectors 104.2 x 104.2 x 126.5 Å. Pore waters were not modelled. The simulation cell consisted of ~112K atoms. Single point mutations were made using CHARMM-GUI to create the V174A, H206S, H206C, H206Y, and H206Q systems. The CHARMM36 force field was used for protein (7, 8), ions, and lipids (9) along with the TIP3P water model (10).

All simulations were performed using GROMACS 2016.3 (11) without modification to the CHARMM-GUI output parameters (with the exception of additional equilibration steps and extended production simulation length). Lennard-Jones interactions were cut off at 1.2 nm and a force-based switching function with a range of 1.0 nm was used. Electrostatic interactions were calculated using particle-mesh Ewald (12, 13) with a real-space cut-off distance of 1.2 nm. Nonbonded interactions were calculated using Verlet neighbor lists (14, 15). All simulations were performed at constant temperature (323.15 K) and pressure (1 atm) using the Nosé-Hoover thermostat (16, 17) with temperature coupling of 1.0 ps and the Parrinello-Rahman

barostat (18, 19) with a time constant of 5.0 ps, respectively. All hydrogen bonds were constrained using the LINCS algorithm (20). The integration time step was 2 fs. All systems followed the standard energy minimization and six-step equilibration procedure of CHARMM-GUI (6), followed by two successive 10 ns protein-restrained simulations conducted in the NPT ensemble. In these equilibration steps, position restraints were applied to main chain backbone atoms and then Cα atoms, with restraint strength of 1000 kJ mol^{-1} nm^{-2}. Thirty simulation repeats were created for WT, V174A, H206S/Q/Y systems with randomized initial velocities for production simulations, with the exception of H206C (ten repeats). Production simulations were conducted for ~400 ns for all simulation repeats for an aggregate total of 67.46 μs.

Prior to analysis, all simulation frames were aligned such that the principal axis formed by TM1 helix Cα atoms were aligned to the box vector *z*. Analysis was performed on all simulation frames spaced at 1.0 ns after removing the first 100 ns of data from each simulation repeat, with the exception of HOLE analysis (21), which was performed on all simulation frames spaced at 20.0 ns after removing the first 100 ns of data. All axial coordinates were measured with respect to the center of mass of the pore helix Cα atoms (residues 141 to 174). Axial histograms of water oxygen atoms, Na^+, and Cl^-, was computed within a cylinder of radius of 10 Å centered at the pore center of mass. Error bars were computed using the standard error of mean over all simulation repeats. Statistical analysis was performed to compare the mean of the radial angle in the WT dataset to all other mutants presented in Fig. *5E*. For our significance test, the average radial angle was extracted from each of the six subunits for all thirty simulation repeats in WT, V174A, H206S/Y/Q and ten simulation repeats for H206C, resulting in 358 and 238 degrees of freedom for our statistical test. The p-value from a two-sided t-test was 2.3×10^{-6}, 4.3×10^{-21}, 4.0×10^{-21}, 1.1×10^{-21}, and 7.0×10^{-6} for WT/V174A, WT/H206S, WT/H206Q, WT/H206Y, WT/H206C, respectively, suggesting that the difference between the mean of these distributions are significant ($P < 0.05$).

An additional set of systems were modelled to test the effect of modifications to temperature and the effect of Na^+ binding on TM1 helix rotation and pore hydration. Both of these models were simulated using a protocol identical to the methodology above with the exception of two parameters. In one system, we simulated WT dOrai1 at

a temperature of 300 K, lower than the other systems in this work (T=323 K). In two more systems, WT and H206S dOrai1, we adjusted the strength of Na^+ binding to E178 carboxylate groups in the molecular dynamics force field. The strength of Na^+ binding was increased by removing the default CHARMM36 parameters that were originally introduced based on osmotic pressure measurements (22). Each of these simulations consisted of ten ~400 ns repeats for each system, for an aggregate total of 12.77 μs. At lower simulation temperatures we observed negligible effects on pore hydration and TM1 helix rotation (***SI Appendix*, Fig. S10)**. We observed that strongly bound Na^+ in the selectivity filter (the E178 ring) had stabilizing effects on the TM1 helices that resulted in lower axial hydration and helix rotation in the WT system (***SI Appendix*, Fig. S10**). Increased propensity for helix rotation and pore hydration were observed in the H206S model, suggesting that our mechanism may be robust to force field choice.

Atomic packing analysis. Atomic packing analysis including explicit hydrogen atoms was carried out using the programs REDUCE and PROBE (23). The PROBE algorithm simulates rolling a 0.25Å radius sphere along the van der Waals surfaces; where the probe sphere contacts two surfaces, each is marked with an indication (a 'dot') that classifies whether the surfaces are in wide contact (>0.25Å apart), close contact (0.25-0.0Å), overlapped (interpenetrating to -0.25Å), and clashing (>-0.25Å). Bad contacts, or clashes, arise from inaccuracies in the model and are found increase with decreasing crystallographic resolution (23). Although the structure of 4HKR was determined at 3.3Å resolution, the distribution of small-probe contact dots nevertheless provides a qualitative measure of the extent and complementarity of local packing interactions. Helix-helix specific contacts were investigated using selection flags available in PROBE (24). The resulting contact dot scores were summed for all atoms of a residue and assigned on a residue-by-residue basis using a script based on ScoreDotsAtAtom (24), then tabulated and displayed using PyMOL.

REFERENCES

1. Prakriya M*, et al.* (2006) Orai1 is an essential pore subunit of the CRAC channel. *Nature* 443(7108):230-233.
2. Navarro-Borelly L*, et al.* (2008) STIM1-Orai1 interactions and Orai1 conformational changes revealed by live-cell FRET microscopy. *J Physiol* 586(22):5383-5401.
3. Zal T & Gascoigne NR (2004) Photobleaching-corrected FRET efficiency imaging of live cells. *Biophys J* 86(6):3923-3939.
4. Hou X, Pedi L, Diver MM, & Long SB (2012) Crystal Structure of the Calcium Release-Activated Calcium Channel Orai. *Science* 338:1308-1313.
5. Fiser A & Sali A (2003) Modeller: generation and refinement of homology-based protein structure models. *Methods in Enzymology* 374:461-491.
6. Jo S, Kim T, & Im W (2007) Automated builder and database of protein/membrane complexes for molecular dynamics simulations. *PLoS One* 2(9):e880.
7. Best RB*, et al.* (2012) Optimization of the additive CHARMM all-atom protein force field targeting improved sampling of the backbone phi, psi and side-chain chi(1) and chi(2) dihedral angles. *J Chem Theory Comput* 8(9):3257-3273.
8. MacKerell AD*, et al.* (1998) All-atom empirical potential for molecular modeling and dynamics studies of proteins. *J Phys Chem B* 102(18):3586-3616.
9. Klauda JB*, et al.* (2010) Update of the CHARMM all-atom additive force field for lipids: validation on six lipid types. *J Phys Chem B* 114(23):7830-7843.
10. Jorgensen WL, Chandrasekhar J, Madura JD, Impey RW, & Klein ML (1983) Comparison of Simple Potential Functions for Simulating Liquid Water. *J Chem Phy* 79(2):926-935.
11. Abraham MJ (2015) GROMACS: High performance molecular simulations through multi-level parallelism from laptops to supercomputers. *Software* X:1-7.
12. Darden T, York D, & Pedersen L (1993) Particle Mesh Ewald - an N.Log(N) Method for Ewald Sums in Large Systems. *J Chem Phys* 98(12):10089-10092.
13. Essmann U*, et al.* (1995) A Smooth Particle Mesh Ewald Method. *J Chem Phys* 103(19):8577-8593.
14. Verlet L (1967) Computer Experiments on Classical Fluids .I. Thermodynamical Properties of Lennard-Jones Molecules. *Phys Rev* 159(1):98-+.
15. Pall S & Hess B (2013) A flexible algorithm for calculating pair interactions on SIMD architectures. *Comput Phys Commun* 184(12):2641-2650.

16. Hoover WG (1985) Canonical dynamics: Equilibrium phase-space distributions. *Phys Rev A Gen Phys* 31(3):1695-1697.
17. Nose S (1984) A Molecular-Dynamics Method for Simulations in the Canonical Ensemble. *Mol Phys* 52(2):255-268.
18. Parrinello M & Rahman A (1980) Crystal-Structure and Pair Potentials - a Molecular-Dynamics Study. *Phys Rev Lett* 45(14):1196-1199.
19. Nose S & Klein ML (1983) Constant Pressure Molecular-Dynamics for Molecular-Systems. *Mol Phys* 50(5):1055-1076.
20. Hess B (2008) P-LINCS: A parallel linear constraint solver for molecular simulation. *J Chem Theory Comput* 4(1):116-122.
21. Smart OS, Neduvelil JG, Wang X, Wallace BA, & Sansom MS (1996) HOLE: a program for the analysis of the pore dimensions of ion channel structural models. *J Mol Graphics* 14(6):354-360, 376.
22. Venable RM, Luo Y, Gawrisch K, Roux B, & Pastor RW (2013) Simulations of Anionic Lipid Membranes: Development of Interaction-Specific Ion Parameters and Validation Using NMR Data. *J Phys Chem B* 117(35):10183-10192.
23. Word JM*, et al.* (1999) Visualizing and quantifying molecular goodness-of-fit: small-probe contact dots with explicit hydrogen atoms. *J Mol Biol* 285(4):1711-1733.
24. Word JM (2000) All-atom small-probe contact surface analysis: An information-rich description of molecular goodness-of-fit. *Ph.D. Thesis, Duke University*.
25. Li Z*, et al.* (2011) Graded activation of CRAC channel by binding of different numbers of STIM1 to Orai1 subunits. *Cell Res* 21(2):305-315.
26. McNally BA, Somasundaram A, Jairaman A, Yamashita M, & Prakriya M (2013) The C- and N-terminal STIM1 binding sites on Orai1 are required for both trapping and gating CRAC channels. *J Physiol* 591(Pt 11):2833-2850.
27. Yamashita M*, et al.* (2017) STIM1 activates CRAC channels through rotation of the pore helix to open a hydrophobic gate. *Nat Comm* 8:14512.

SUPPLEMENTARY FIGURES

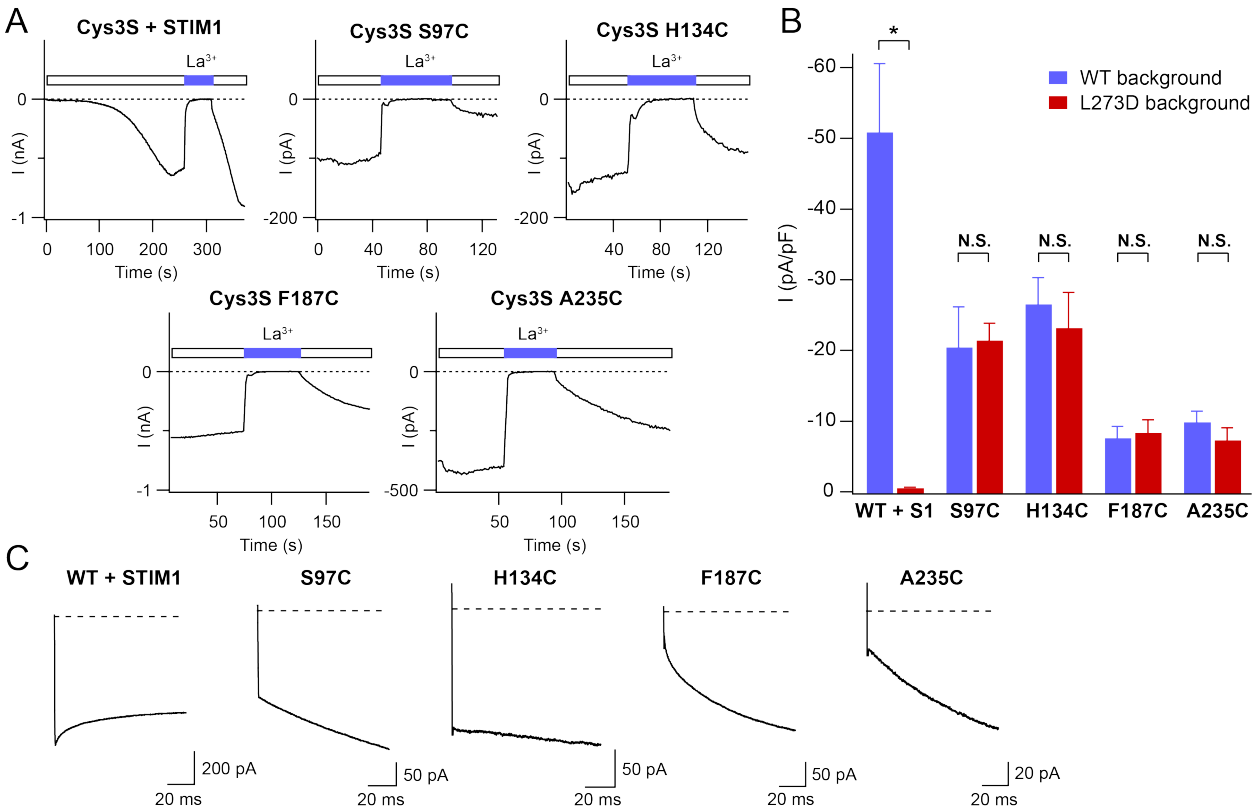

Figure S1. GOF phenotypes of constitutively open cysteine mutants are independent of local disulfide bond formation or enhanced STIM1 binding. (*A*) Cysteine mutants S97C, H134C, F187C, and A235C remain constitutively active in the Cys3S background in which the three endogenous Orai1 cysteine residues have been replaced by serines. **(*B*)** Current amplitudes of GOF cysteine mutants are unaffected in the L273D background which abrogates STIM1 binding to Orai1 (25, 26). N = 4-7 cells. Values are mean ± S.E.M. *P < 0.05. **(*C*)** Unlike WT Orai1 activated by STIM1, GOF cysteine mutants do not exhibit Ca^{2+}-dependent fast inactivation, consistent with the ability for these mutants to conduct current independently of STIM1 binding.

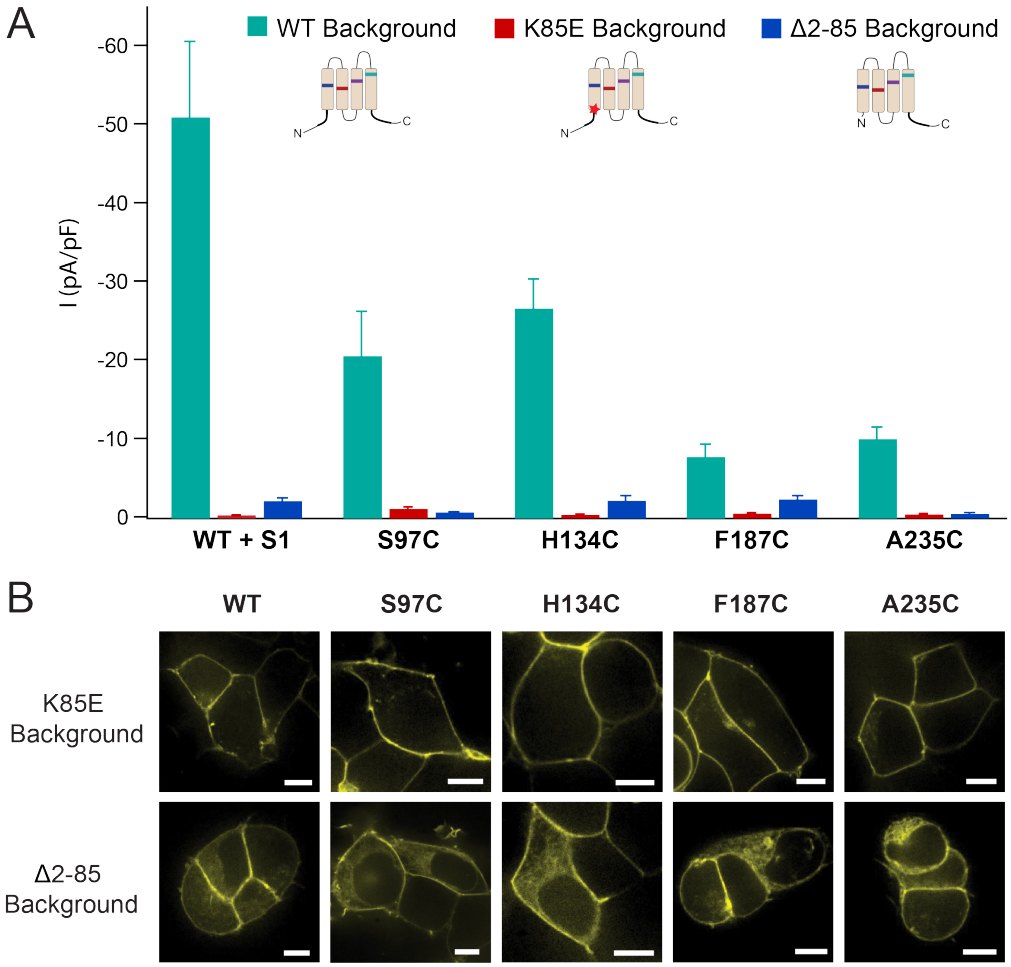

Figure S2. Mutations of the Orai1 N-terminus abolish activity of the constitutively open TM1-4 mutants. (*A*) Current densities of constitutively open cysteine mutants S97C, H134C, F187C, and A235C in WT, K85E, or N-terminal truncation Δ2-85 backgrounds. K85E and Δ2-85 both abrogate the activity of these GOF channels. **(*B*)** Confocal images of WT Orai1-YFP and cysteine mutants S97C, H134C, F187C, and A235C in the K85E and Δ2-85 backgrounds. K85E Orai1-YFP constructs are well expressed in the membrane. Some fluorescence is seen in a cytosolic compartment in the Δ2-85 channels, but good expression is still retained in the plasma membrane. (Scale bars: 10 μm.)

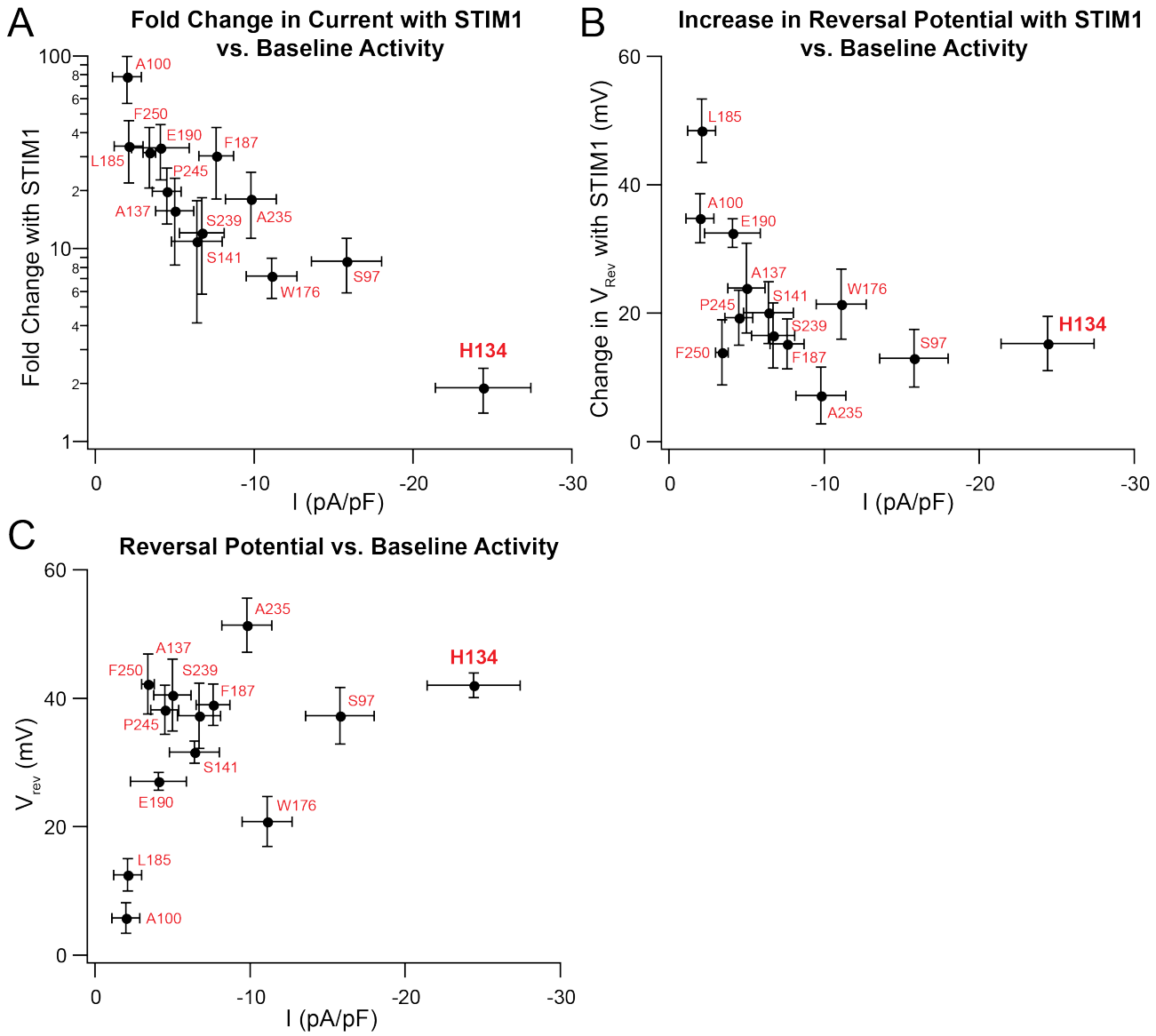

Figure S3. Differential modulation of GOF cysteine mutants by STIM1. (*A*) Plot of the fold change in current of GOF cysteine mutants in the presence of STIM1 versus current density in the absence of STIM1. The fold increase in current following whole-cell break-in was calculated by measuring the peak of the STIM1-gated current amplitude at 300 s or later divided by the amount of constitutive current seen at the time of whole-cell break-in (t=0). ER Ca^{2+} stores were passively depleted by 8 mM BAPTA in the internal solution. Weakly active mutants can be further activated by STIM1, while mutants that are strongly open at baseline such as H134C are not significantly boosted. **(*B*)** STIM1 increases the Ca^{2+} selectivity of open mutants as reflected in the reversal potential. Increases in V_{rev} by STIM1 are inversely related to the baseline activity of GOF cysteine mutants. **(*C*)** H134C is the most strongly activating mutation based on the dual

criteria of a large pre-activated current and very positive reversal potential at the time of whole-cell break-in relative to other GOF cysteine mutants. The leaky gate mutations, F99C and V102C, were excluded from these plots because they are constitutively permeant due to disruption of the gate itself in contrast to the activating mutations in TMs 2-4.

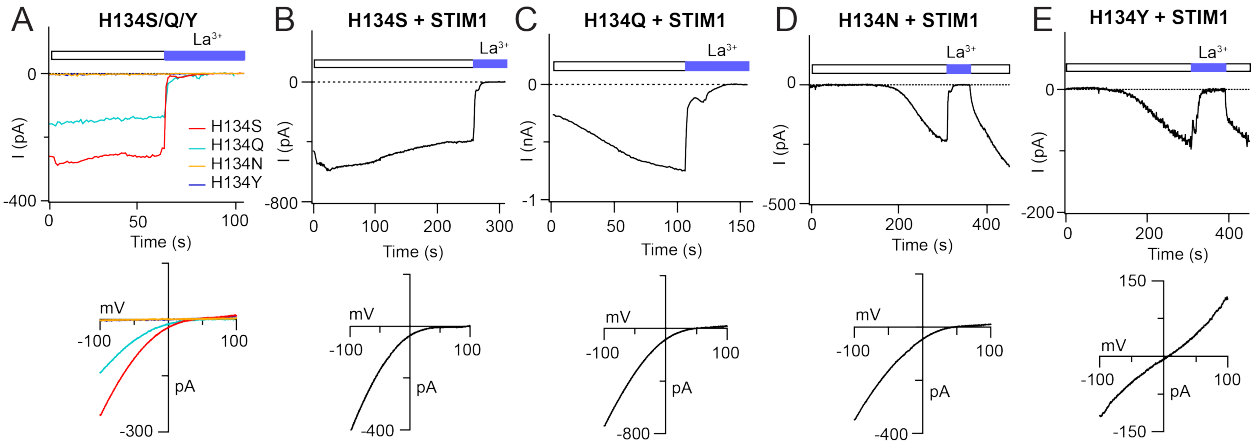

Figure S4. Analysis of H134X mutants in the absence and presence of STIM1. (*A*) H134S and H134Q Orai1 channels are constitutively active while H134N and H134Y channels are not open without STIM1. **(*B*)** Co-expression of STIM1 with H134S does not increase Orai1 current following whole-cell break-in. **(*C*)** Partially active H134Q mutant channels exhibit store-operated gating following whole-cell break-in indicating that they can be further activated by STIM1. **(*D*)** H134N channels are store-operated and Ca^{2+}-selective, similar to WT channels. **(*E*)** STIM1-mediated gating of H134Y channels is impaired as seen by the slow induction of a non-selective current following whole-cell break-in. Bottom panels show current-voltage relationships of the respective mutants.

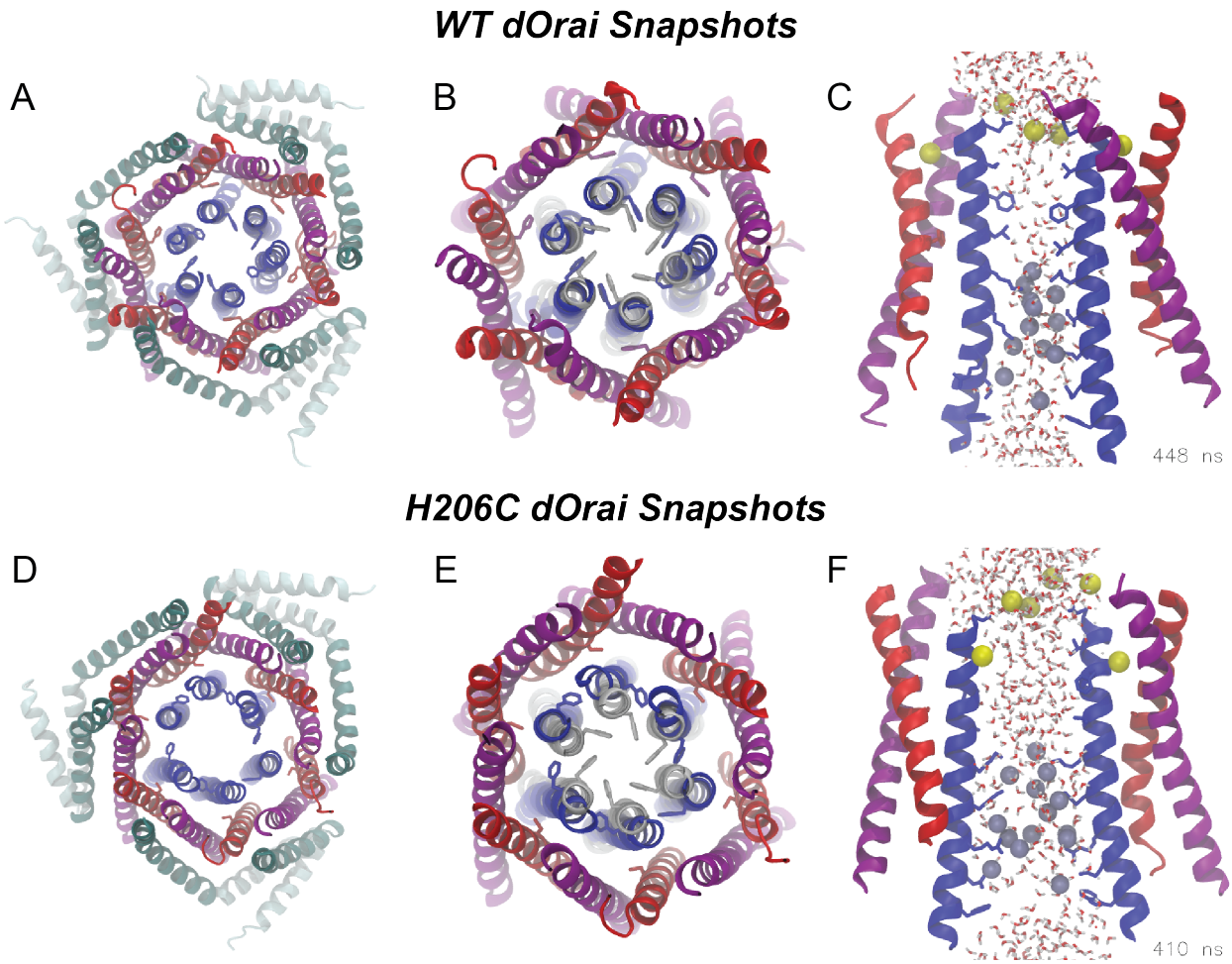

Figure S5. Snapshots of MD simulations of WT and H206C dOrai channels. ***(A-C)*** Snapshots of WT dOrai at 448 ns and ***(D-F)*** H206C dOrai at 410 ns. TMs 1-4 are colored in blue, red, purple and teal respectively, with the positions of residues F171 (blue) and H206 (red) shown as sticks. Intracellular and extracellular loops are not depicted. ***(A, D)*** Top views of the entire channel. ***(B, E)*** Top views of TMs 1-3. The crystallographic structure of dOrai TM1 and F171 side chains are shown as a reference in white. ***(C, F)*** Side views of TM1 to TM3 for two diagonal subunits depicting water and ionic occupancy of the pore. All pore-lining side chains are depicted as sticks (from top to bottom; E178, V174, F171, L167, K163, R155, Q152, and W148). Na^+ and Cl^- ions are rendered as yellow and dark blue spheres respectively. Water molecules are shown as gray/red sticks within a cylinder centered along the central pore axis.

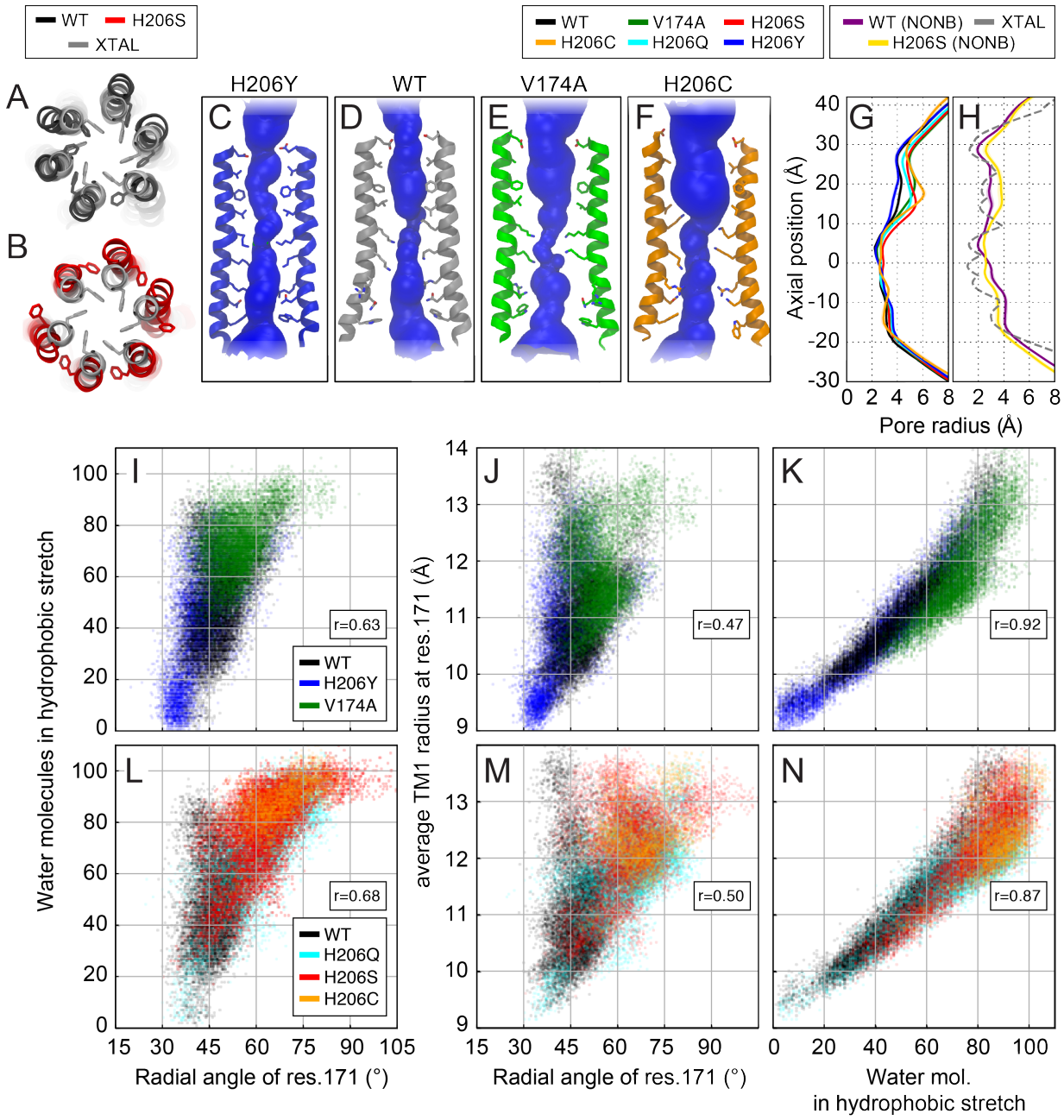

Figure S6. Analysis of TM1 dilation, hydration, and rotation from molecular dynamics simulations. (*A-B*) Comparison of simulation snapshots of WT (black) and H206S (red) models at t=350 ns and the crystallographic structure of dOrai1 (white). **(*C-F*)** Pore profiles computed using HOLE from the H206Y, WT, V174A, and H206C models from snapshots taken at t=350 ns. All water molecules and ions within the pore were removed for this analysis, and only two diagonal subunits are visualized. **(*G*)** Average pore radius for WT (black), V174A (green), and H206S/C/Q/Y (red, orange, aqua, blue) computed using HOLE for snapshots selected from dt=20ns across all simulation repeats. Shaded regions depict values ± S.E.M. **(*H*)** Average pore

radius for WT (No NBFIX), H206S (No NBFIX), and the crystallographic structure of dOrai1. The axial coordinate system used for HOLE profiles of panels (G-H) is in agreement with those used for hydration profiles in Fig. 5C. **(*I, L*)** The relationship between the number of water molecules in the hydrophobic stretch (10-25 Å) and the mean radial angle of residue 171 (defined as the angle between the center of mass of the two helical turns centered at residue 171, and the Cα atom of residue 171) over all subunits. At small values of the residue 171 radial angle, the number of water molecules in the hydrophobic stretch is geometrically constrained, but with increased radial angle, the number of pore waters can vary significantly across a wide range. **(*J, M*)** The relationship between the average radius of the of the pore at residue 171 (defined as the distance in the X-Y plane from the pore center of mass to the center of mass of residues 167-175 Cα atoms, averaged over all subunits) to the mean radial angle of residue 171. **(*K, N*)** The correlation between average radius of the pore at residue 171 and the number of water molecules in the hydrophobic stretch. For all scatter plots, each point corresponds to data taken at an individual simulation snapshot, from all snapshots spaced at dt=1 ns for WT (black), V174A (green), and H206S/C/Q/Y (red, orange, aqua, blue) models. Pearson correlation coefficient is shown as an in-set in panels ***I-M***.

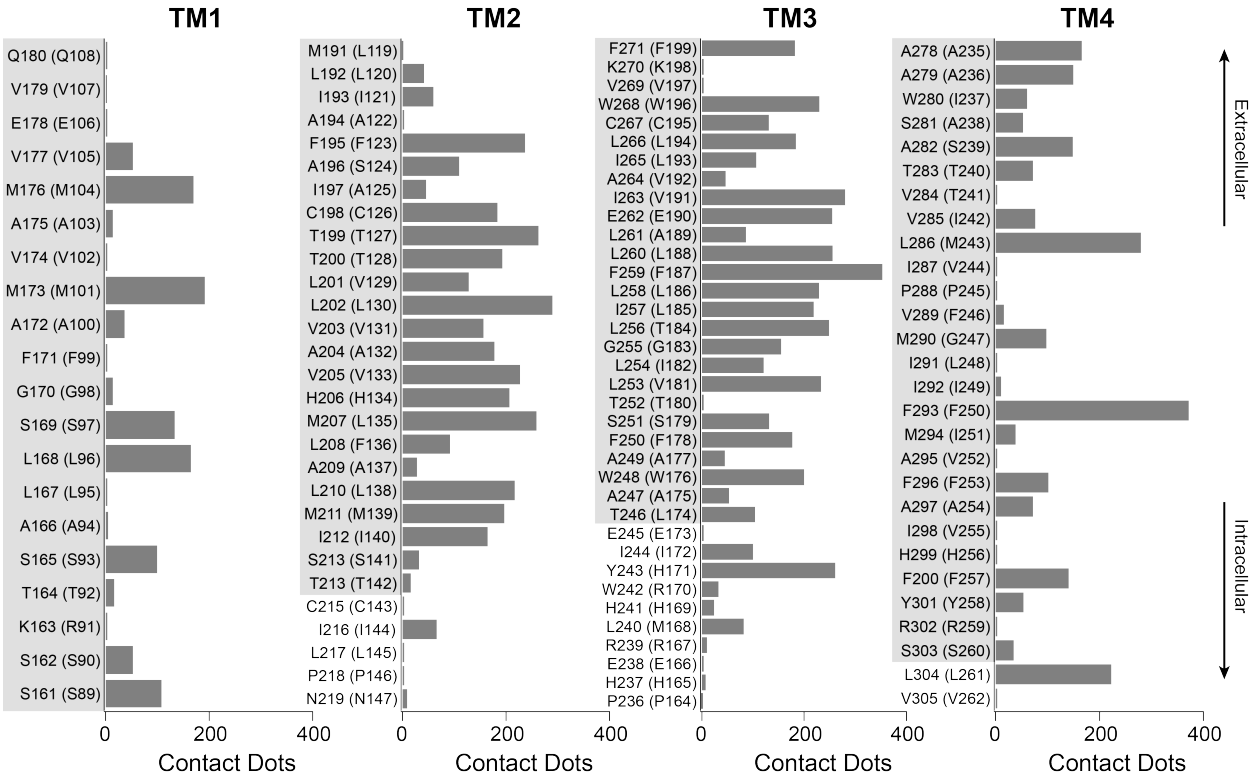

Figure S7. Atomic packing analysis of all transmembrane residues in dOrai. The total number of contact dots per residue measured for each transmembrane amino acid in the hexameric dOrai crystal structure including intramolecular and intermolecular neighbors. Residues in TMs 2 and 3 make more contacts with their neighbors compared to those in TMs 1 or 4, suggesting that they are more tightly packed.

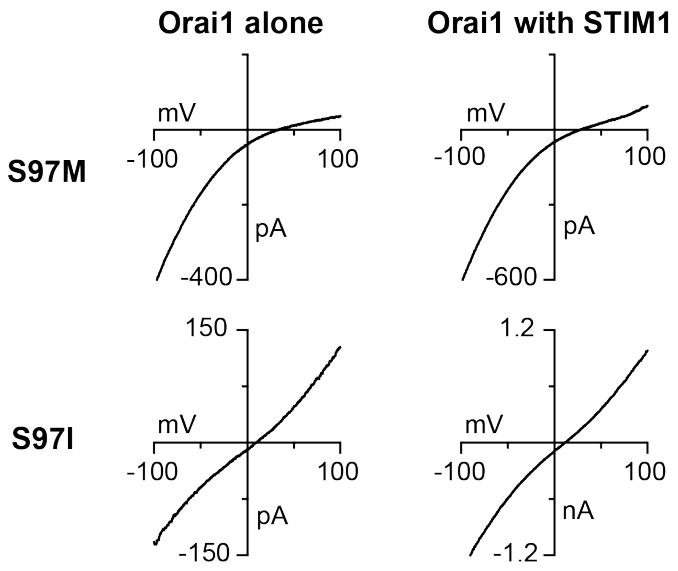

Figure S8. The Ca^{2+} selectivity of the constitutively conducting S97M and S97I mutants is not enhanced by STIM1. I-V relationships of S97M and S97I mutants in the absence and presence of STIM1. Unlike most other GOF mutants, STIM1 does not significantly enhance the reversal potential of these mutant channel I-Vs.

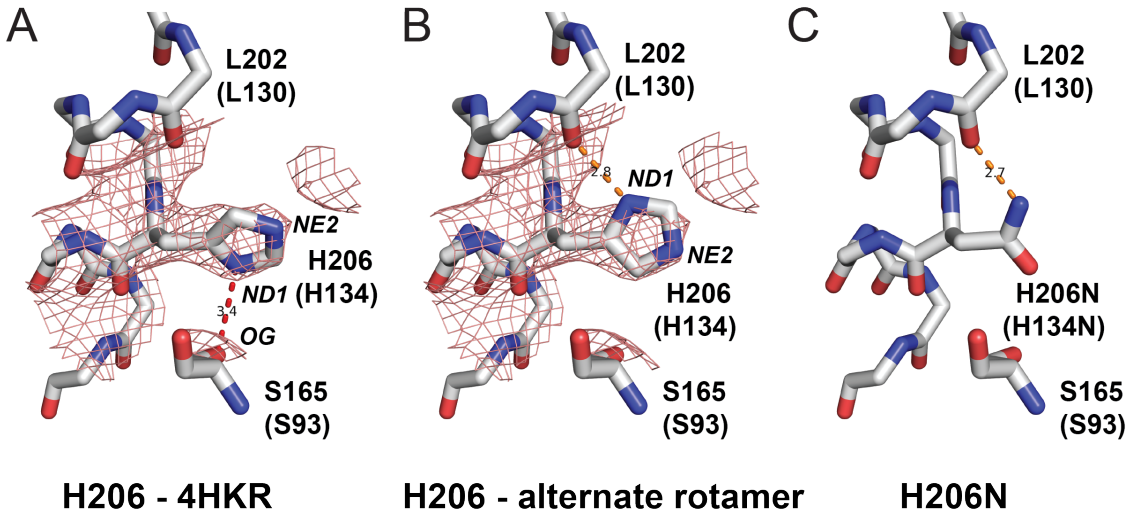

Figure S9. Alternate rotamer of H206 and H206N may interact with the TM2 backbone carbonyl to stabilize its conformation at the TM1-TM2 interface. (*A*) Electron density of 4HKR superimposed with the H206 side chain as built in the 4HKR structure with the assigned χ_1, χ_2 angles of -82°, -60°. In this rotamer, the ND1 nitrogen of the imidazole ring may interact with S165 (3.4 Å). The map is contoured at 1.5σ. **(*B*)** Alternate rotamer of H206 with χ_1, χ_2 angles of -82°, 80° is also consistent with the electron density of 4HKR and allows hydrogen bonding (2.8 Å) between the ND1 nitrogen with the backbone carbonyl of L202 one turn preceding it. **(*C*)** In an H206N substitution, the side chain can also adopt a rotameric configuration allowing hydrogen bonding between the ND2 nitrogen and the carbonyl oxygen (2.8 Å) of L202, thereby possibly stabilizing it in a similar configuration towards the TM1-TM2 interface. hOrai1 numbering is indicated in parentheses.

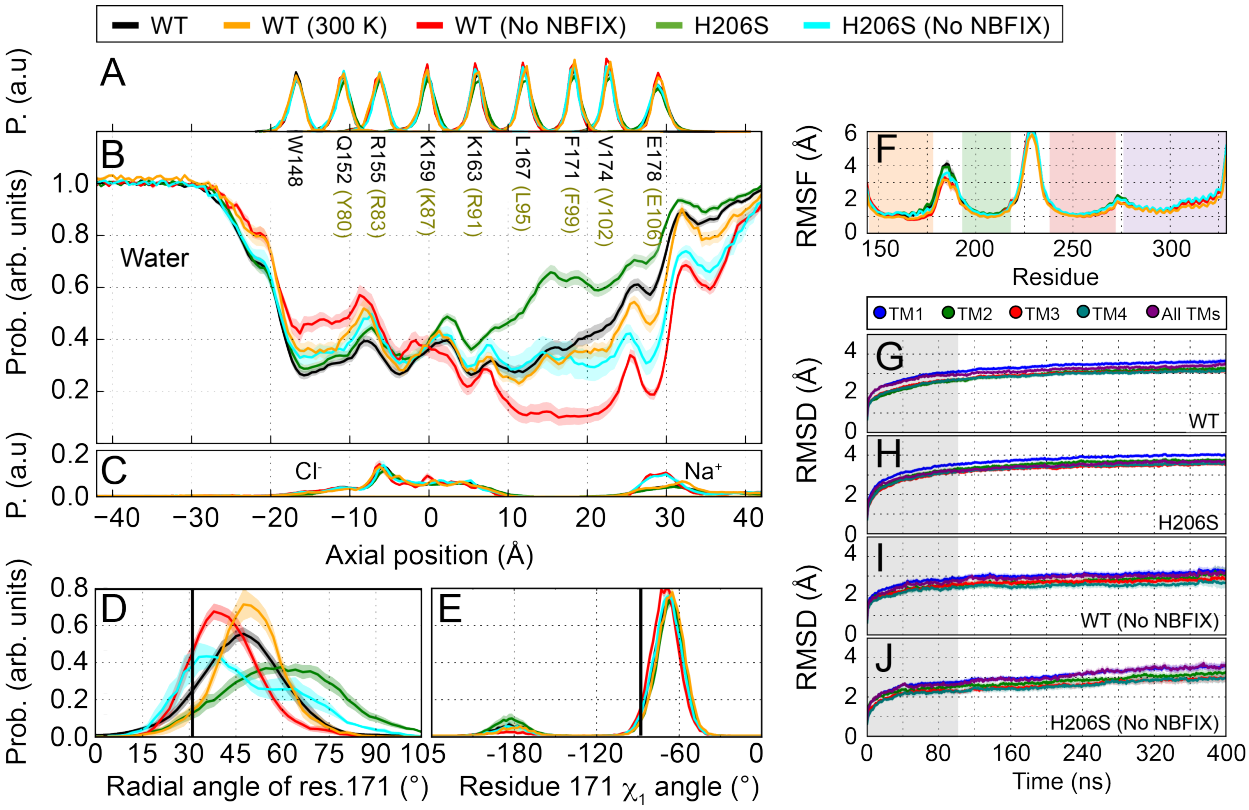

Figure S10. Pore helix rotation and hydration occur with modified temperature and ion interaction strength in MD simulations. Data in panels A-J compare the WT and H206S models presented in Fig. 5, to those conducted in two different simulation conditions; a temperature decrease from T=323 K (black) to T=300 K (orange) in the WT model, and with a single force field modification to increase sodium-carboxylate interaction strength, referred to as "No NBFIX", for WT (red) and H206S (aqua). **(*A*)** Average distributions of the axial position of Cα atoms for all pore-lining residues. The residues corresponding to human Orai1 are shown in brown. Data in panels A-H were computed using an alternate molecular model of WT dOrai1 in three simulation conditions; T=323 K (black), T=300 K (green), and T=323K, with "No NBFIX" (red). Average distribution of **(*B*)** water oxygen atoms and **(*C*)** Na^+ and Cl^- ions along the pore axis. Temperature reduction had minor effects on the axial distribution of water and ions. Molecular simulations analyzed in Fig. 5 include a revised parameter that reduces sodium-carboxylate interaction strength. Previous molecular simulations in Yamashita *et al.* (27) did not include this revised parameter, and we have presented results here to examine the effect of this parameter on pore rotation and hydration ("No NBFIX"). Unmodified interaction strength resulted in greater occupancy of Na^+ near E178, and reduced hydration in the hydrophobic section of the

pore with respect to the reduced strength force field, similar to the hydration profiles results presented in Yamashita *et al.* (27). **(*D*)** Average distribution of the radial angle of residue 171 defined as the angle between the center of mass of the two helical turns centered at residue 171, and the Cα atom of residue 171. The means of these distributions over all simulation repeats in degrees is 47 ± 1 for WT, 50 ± 1 for WT (300 K), 42 ± 2 for WT (No NBFIX), 61 ± 1 for H206S, and 48 ± 2 for H206S (No NBFIX). The radial angle in the crystallographic structure (31°) is shown as a black vertical bar for reference. **(*E*)** Average distribution of side chain torsion χ_1 of residue 171 in the three simulation conditions. The χ_1 of residue 171 in the crystallographic structure (-88°) is shown as a black vertical bar for reference. **(*F*)** Average root mean square fluctuations of Cα atoms over all simulation repeats and subunits, for each residue of the dOrai1 subunit. Primary alpha helical regions are indicated as shaded bars. **(*G-J*)** Average root mean square deviation (RMSD) from the dOrai crystallographic structure for each system as a function of simulation time, for individual TM segments (TM1-TM4) and all TM segments. A gray shaded region indicates the portion of data removed for equilibration.

Movie S1. MD simulation of WT dOrai. Multiple synchronized molecular renderings of a single simulation repeat (0 to 448 ns). Depictions of the channel are as described for Fig. S9. Na^+ and Cl^- ions are rendered as yellow and dark blue spheres respectively. Water molecules are shown as gray/red sticks within a cylinder centered along the central pore axis.

Movie S2. MD simulation of H206C dOrai. Multiple synchronized molecular renderings of a single simulation repeat (0 to 428 ns). Depictions of the channel are as described for Fig. S9. Na^+ and Cl^- ions are rendered as yellow and dark blue spheres respectively. Water molecules are shown as gray/red sticks within a cylinder centered along the central pore axis.

Table S1: Current densities and reversal potentials of GOF cysteine mutations in TMs 1-4.

		Orai1 alone		Orai1 with STIM1	
		Current Density (pA/pF ± SEM)	Reversal Potential (mV ± SEM)	Fold Change in Current with STIM1 (Ratio ± SEM)	Reversal Potential (mV ± SEM)
	WT	-0.2 ± 0.02	*	1033 ± 568	52.3 ± 2.8
TM1	**S97C**	-15.8 ± 2.2	37.3 ± 4.4	9 ± 3	50.3 ± 0.9
	F99C	-3.4 ± 0.7	11.9 ± 3.9	ND	ND
	A100C	-2.0 ± 0.9	5.8 ± 2.4	78 ± 21	40.5 ± 3.4
	V102C	-37.5 ± 8.2	27.2 ± 2.6	ND	ND
TM2	**H134C**	-24.4 ± 3.0	42.0 ± 1.9	2 ± 0.4	57.2 ± 3.7
	A137C	-5.0 ± 1.2	40.5 ± 5.6	16 ± 7	64.4 ± 4.1
	S141C	-6.4 ± 1.6	31.6 ± 1.7	11 ± 7	51.7 ± 4.6
TM3	**W176C**	-11.1 ± 1.6	20.8 ± 3.9	7 ± 2	42.2 ± 3.7
	L185C	-2.1 ± 0.9	12.5 ± 2.5	34 ± 12	60.9 ± 4.3
	F187C	-7.6 ± 1.1	39.0 ± 3.2	30 ± 12	54.1 ± 2.3
	E190C	-4.1 ± 1.8	27.1 ± 1.4	33 ± 11	59.6 ± 1.8
TM4	**A235C**	-9.8 ± 1.6	51.4 ± 4.2	18 ± 7	58.7 ± 1.2
	S239C	-6.7 ± 1.4	37.3 ± 5.1	12 ± 6	53.9 ± 3.1
	P245C	-4.5 ± 0.9	38.2 ± 3.8	20 ± 6	57.5 ± 2.2
	F250C	-3.4 ± 0.4	42.2 ± 4.7	32 ± 11	56.1 ± 1.9

GOF cysteine mutations exhibit varying levels of current amplitudes and ion selectivity. Current amplitudes were measured during step pulses to -100 mV and reversal potentials were measured during ramps applied from -100 to 100 mV. In cells co-expressing STIM1, ER Ca^{2+} stores were passively depleted by 8 mM BAPTA in the internal solution. The fold increase in current following whole-cell break-in was calculated by measuring the peak of the STIM1-gated current amplitude at 300 s or later divided by the amount of constitutive current seen at the time of whole-cell break-in (t=0). N = 4-16 cells. *not measured due to small current amplitudes (<2 pA/pF). ND = not determined.

Table S2: Current densities and reversal potentials of H134X mutations.

	Orai1 alone		Orai1 with STIM1	
	Current Density (pA/pF ± SEM)	Reversal Potential (mV ± SEM)	Fold Change in Current with STIM1 (Ratio ± SEM)	Reversal Potential (mV ± SEM)
H134A	-17.3 ± 3.0	49.1 ± 4.2	1 ± 0.1	59.9 ± 3.3
H134C	-24.4 ± 3.0	42.0 ± 1.9	2 ± 0.4	57.2 ± 3.7
H134E	-11.1 ± 4.2	52.4 ± 5.5	7 ± 3	61.0 ± 1.7
H134F	-0.4 ± 0.3	*	28 ± 11	12.4 ± 2.4
H134G	-1.5 ± 0.2	*	19 ± 6	59.7 ± 6.6
H134I	-1.2 ± 0.2	*	23 ± 7	13.6 ± 4.6
H134K	-0.3 ± 0.2	*	*	*
H134L	-1.4 ± 0.3	*	20 ± 11	8.8 ± 1.4
H134M	-18.5 ± 2.7	51.2 ± 4.3	15 ± 6	56.5 ± 3.9
H134N	-0.2 ± 0.02	*	268 ± 80	55.1 ± 4.2
H134P	-12.7 ± 3.7	48.0 ± 8.6	1 ± 0.1	52.4 ± 3.7
H134Q	-4.9 ± 1.3	53.1 ± 1.6	11 ± 3	54.3 ± 3.9
H134S	-29.7 ± 3.4	46.6 ± 4.3	1 ± 0.1	61.3 ± 2.9
H134T	-17.6 ± 2.4	51.9 ± 5.5	1 ± 0.1	53.6 ± 5.8
H134V	-12.1 ± 2.6	18.3 ± 2.0	13 ± 3	56.7 ± 8.1
H134W	-0.2 ± 0.1	*	*	*
H134Y	-0.1 ± 0.03	*	155 ± 44	8.3 ± 1.0

Different H134 substitutions give rise to currents with different degrees of constitutive activity and ion selectivity. Current amplitudes, reversal potentials, and fold change in current amplitude with STIM1 were determined as described in Table S1. N = 5-12 cells. *not measured due to small current amplitudes (<2 pA/pF).

Table S3: Current densities and reversal potentials of S97X mutations.

	Orai1 alone		Orai1 with STIM1	
	Current Density (pA/pF ± SEM)	Reversal Potential (mV ± SEM)	Fold Change in Current with STIM1 (Ratio ± SEM)	Reversal Potential (mV ± SEM)
S97A	-0.2 ± 0.1	*	107 ± 46	51.8 ± 3.6
S97C	-20.4 ± 5.7	38.4 ± 5.7	8 ± 3	50.3 ± 0.9
S97F	-0.8 ± 0.3	*	12 ± 4	30.0 ± 3.3
S97G	-0.7 ± 0.2	*	79 ± 58	61.2 ± 3.2
S97H	-1.1 ± 0.4	*	32 ± 18	18.3 ± 2.6
S97I	-23.2 ± 4.4	7.3 ± 0.7	6 ± 1	9.8 ± 2.1
S97L	-29.9 ± 7.5	31.7 ± 5.3	2 ± 1	32.9 ± 3.1
S97M	-44.7 ± 7.3	27.9 ± 4.1	1 ± 0.1	33.3 ± 6.3
S97N	-1.7 ± 0.5	*	37 ± 18	19.0 ± 3.2
S97Q	-1.4 ± 0.1	*	53 ± 14	28.6 ± 3.4
S97T	-0.9 ± 0.3	*	112 ± 27	46.8 ± 5.1
S97V	-6.9 ±1.6	8.9 ± 0.8	20 ± 7	11.9 ± 1.3
S97W	-0.1 ± 0.03	*	*	*
S97Y	-2.7 ± 0.7	14.3 ± 3.8	2 ± 1	16.3 ± 4.4

S97X mutants display varying levels of constitutive activity and ion selectivity. Current amplitudes, reversal potentials, and fold change in current amplitude with STIM1 were determined as described in Table S1. N = 4-8 cells. *not measured due to small current amplitudes (<2 pA/pF).